

Supplementary Information for

Strong and highly variable push of ocean waves on Southern Ocean sea ice

Justin E. Stopa, Peter Sutherland, and Fabrice Ardhuin

Corresponding Author Justin E. Stopa
E-mail: justin.stopa@ifremer.fr

This PDF file includes:

- Supplementary text
- Figs. S1 to S6
- Table S1
- References for SI reference citations

Supporting Information Text

Sentinel-1 analysis and processing

Wave orbital velocities create wave-like features in SAR images because pixels are misplaced in azimuth by a distance that is proportional to the (nearly vertical) line of sight velocity. In ice-covered waters, short random waves are strongly attenuated (1). As a result, bright lines appear in SAR imagery over sea ice that would be blurred if the short wave amplitude was higher (2). When such patterns are present, the dominant peak in the power spectrum of the image intensity yields the dominant wavelength and wave direction (3). The image intensity corresponds to the convergence of vertical velocities along azimuth lines. In the absence of leads and other patterns in the image, the intensity can be inverted into a map of wave orbital velocities, from which a wave spectrum is estimated (4). This inversion is most simple when a single narrow-band swell is dominant, and when the SAR imaging coefficient (5),

$$C_{AR} = k_y U Z / V \quad [1]$$

is within the linear SAR regime, with $C_{AR} < 1.0$ (4). Here k_y is the wavenumber in the azimuth direction, U is the orbital velocity amplitude, Z is the satellite altitude, and V is the satellite velocity. We estimate a unique wave propagation direction by using the phase information computed from a cross-spectrum produced from multiple "looks" following (6).

We use data from both platforms Sentinel-1A (2014-2016) and Sentinel-1B (2016). The wave mode images used in this study are the highest resolution mode of the Sentinel-1 SARs with a spatial resolution of 4 m. Images are acquired every 100 km, alternating between 23 and 37 degree incidence with a repeat cycle of 12 days. An example track is provided in Figures S1 with example roughness images in Figures S2 and S3. Data acquired along the same satellite track give synoptic observations near the ice edge in open water and within the ice pack within a small time window (typically < 30 s). For each track across the marginal ice zone (MIZ), there are typically one and sometimes two images that meet our conservative criteria of a single swell system within the linear regime ($C_{AR} < 0.7$).

We provide an example S1A track in Figures S2 and S3. The overview of the ice concentration in Figure S1 shows the S1A acquisitions across the MIZ. We provide pertinent geophysical information in Table S1. Images I and II (Figure S2) are furthest from the ice edge (> 500 km) and show no signatures of ocean waves and the SAR inversion was not performed. Images III and IV (Figure S2) show clear ocean wave signatures; the large-scale variations in backscatter are expected to be related to sea ice and/or snow features. These SAR acquisitions are within the linear imaging regime and the estimates of $H_s \simeq 0.6$ m for both images are expected to be accurate since $C_{AR} < 0.7$. Image V (Figure S3) has clear wave signatures but some wave crests cannot be uniquely mapped ($C_{AR} > 0.7$). We did not include this image within our dataset but the estimate $H_s = 1.65$ m is reasonable. Image VI (Figure S3) contains wave features but the wave signatures cannot be uniquely mapped ($C_{AR} = 1.25$), so the H_s cannot be trusted. This image contains a mix of ocean and sea ice; where the lighter region is expected to be ice free and the darker region is sea ice. Images VII and VIII (Figure S3) are open ocean with only subtle ice features in image VII. Notice the azimuth cutoff is large and swell is distorted by the presence of high frequency waves. The empirical wave heights estimated of (7) are slightly larger than those of the numerical wave model.

This variety of wave and ice features makes it difficult to interpret images based on statistical parameters alone. For that reason, each satellite track was visualized to verify that the SAR image was indeed ice-covered and that distinct wave signatures are present. It remains challenging to make an automated detection system that properly separates wave and ice features (8). In most tracks we are able to obtain one image for which the inversion algorithm gives unambiguous results, sometimes two, as in the example above.

The open ocean sea state in the Southern Ocean is typically very active with average values of H_s around 4.5 m in the Indian Ocean sector, 4 m for the Pacific and 3.5 m for the Atlantic. This gives waves that generally propagate a few hundred kilometers in the MIZ with wave heights above 0.5 m, giving a high probability the Sentinels will acquire images with waves signatures. This allowed us to obtain data all around the Antarctic continent (see Figure S4). The maximum number of observations are located in the Pacific basin and there is a minimum number of observations in the Weddell Sea that is partially sheltered from swells by the Antarctic peninsula. The position of SAR observations relative to the ice edge range of 25 to 650 km (Figure S4b) demonstrating that waves affect a large region of the MIZ. The majority of the open ocean conditions have $3 < H_s < 5$ m and the largest event in our database reaches 12 m (Figure S4c). Since our SAR inversion algorithm only works for linearly imaged scenes (4) most in-ice conditions have $H_s < 3$ m, and the majority of the observations have $H_s < 1$ m (Figure S4d). These wave spectra derived from the SAR imagery in sea ice are the basis of this study. This dataset is unique because it contains a wide range of sea state and presumably ice conditions for all months, around the entire Southern Ocean.

The SAR inversion is performed using 50% overlap on 2×2 km tile of the original 20×20 km image. This corresponds to a 512×512 (or $2^9 \times 2^9$) tile which is convenient for applying a Fast Fourier Transform. Because our inversion algorithms assume that all the patterns in the image are due to wave orbital motions, it is important to select tiles with minimal ice features such as leads or inhomogeneous snow cover. Therefore a homogeneity test is performed on each tile to ensure that consistent backscatter is present (9). The homogeneity test has also been useful in deciphering wave, ice, and open ocean features in the Arctic marginal ice zone (8). Note that the estimation of the total wave energy is independent of the mean backscatter. Consistent backscatter is only important within each analyzed tile. To use a SAR image, we require that at least 25% of the tiles pass the homogeneity test, giving approximately 50 quality tiles. We then compute the total energy for each tile j from the spectrum F , within the SAR image

$$E_j = \int_{-0.8}^{0.8} \int_{-0.8}^{0.8} F(k_x, k_y) dk_x dk_y, \quad [2]$$

which then gives an estimate $H_{s,j} = 4\sqrt{E_j}$ for each tile. Each image is classified as having 1 or 2 swells since the SAR inversion method works on both (4); however, in our analysis we include SAR images with only single swell systems present.

Images like Figure 1a of the main text that have strong attenuation are analyzed separately. For those images, we set the criteria that the wave height must decay at least 0.5 m across the image. We have a total of 92 images that meet this criteria. In these cases, the attenuation is calculated using the first wave height along the wave propagation direction. To reduce the variability the relative distance is decimated and wave heights at common distances are averaged. The stress calculation in Equation 3 of the Methods is calculated using the decimated data. Finally the average of the stresses is used as a representative value of the image.

All other images, similar to Figure 1d of the main text, must have a nearly stable $H_{s,j}$ across the image and we require the standard deviation of $H_{s,j}$ to be less than 20 cm and an inter-quartile range less than 30 cm. For this group of data (N=2145) we use the median of $H_{s,j}$ to represent the in-ice SAR wave energy. The off-ice wave energy is calculated using the SAR image closest to a point found by back-propagating the waves at the dominant direction along a great circle route and finding the intersection with the 15% ice concentration contour defined by the Special Sensor Microwave Imager (SSM/I) (10). This represents the distance from the ice edge the wave has traveled (x in Equation 3 of the Methods). The off-ice H_s is calculated by an empirical method originally developed for the European Remote Sensing Satellite (ERS2) (11, 12) and Envisat (13). Here we use an adaptation for Sentinel-1 (7).

This method performs well for $H_s \leq 7$ m. For $H_s \geq 8$ m, which corresponds to 2.5% of the dataset used here, wave heights are underestimated, with a relative bias that reaches -15% for $H_s = 12$ m and can be important for other applications. We did not correct for this bias as it only affects few data points and would not change our conclusions. Further, we have also estimated wave attenuation using numerical wave model output (14) instead of the empirical SAR-derived wave heights, and this also gave the same conclusions.

The question of stationarity arises especially for the cases several hundred kilometers from the ice edge. For example a 16-second-wave has group velocity of 12.5 m s^{-1} and it will take 11 hours to propagate 500 km. We used the wave model to assess this impact. First we back-propagate the in-ice SAR observations along great circle routes to the ice edge and then co-locate this time-space location with the wave model. For reference we reproduced Figure 2 of the main text here in Figure S5 and find minimal difference. Furthermore there was no distinguishable difference in Figure 3 of the main text. We prefer to use the empirical SAR observations as the off-ice reference in order to keep the results based on observations.

The in-ice SAR measurements have various distances from the ice edge, therefore it is necessary to estimate the wave stress over common MIZ distances to make a consistent measurement. We make use of the fact that the wave energy decays exponentially (Figure 2 of the main text) (15, 16) to extrapolate our SAR observations to the wave energy at various distances from the ice edge. First we solve for the attenuation rate, α , by applying our off-ice energy E_0 , observed in-ice wave energy $E(x)$, and observed distance x ,

$$E(x) = E_0(x_0)exp[-\alpha x]. \quad [3]$$

Then we use the same exponential relation to extrapolate our SAR observations to arbitrary distances from the ice edge, e.g. 10, 50, and 200 km as in Figure 3 of the main text.

Wave attenuation

It is interesting to compare our wave decay estimates with the few previous measurements available (1, 15–17). In Figure S6 we reproduce the format of Figure 1 in (16), and show the gradient in wave height dH_s/dx estimated as $-\alpha H_s/2$, as a function of the wave height H_s . This includes Figure S6(a) the 2145 cases that use the off-ice wave height $H_{s,0} = 4\sqrt{E_0}$ as reference and Figure S6(b) the 92 cases that have a strong decay within a SAR image.

The median of our results is consistent with (16) for $H_{s,0} < 2$ m. For higher wave heights we find a larger decay. This difference can come from our use of $H_{s,0}$ estimates in open water, while (16) used $H_{s,0}$ estimated in the ice, with values presumably lower. Also their estimate of $dH_s/dx \simeq (H_{s,0} - H_{s,1})/(x_1 - x_0)$ tends to give lower values than our exponential fit. This finite difference estimate also tends to give lower values for the larger $H_{s,0}$ that are measured close to the edge. Still, in spite of these differences, our data also support a weaker decay for higher wave heights, and can be fitted as follows

$$\frac{dH_s}{dx} = -3.00 \times 10^{-6} H_s. \quad [4]$$

The origin of that behavior is not known and nonlinear wave-wave interactions were invoked by (16). We note that another possible nonlinear effect is the floe size distribution of the ice. Indeed, unbroken ice may cause a strong dissipation of wave energy (due to anelastic or inelastic processes for example), that does not happen anymore when the ice is broken by larger waves.

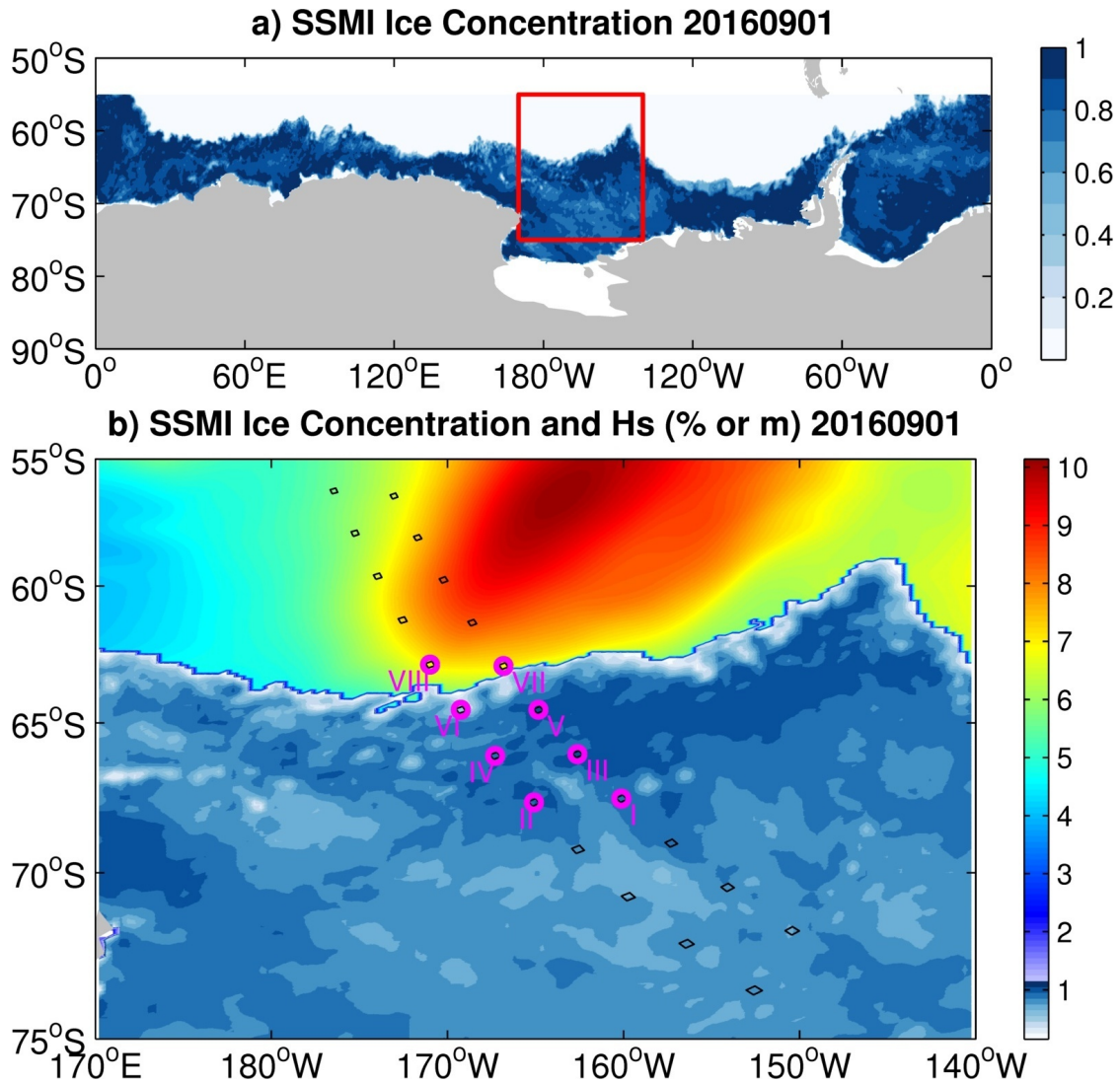


Fig. S1. Ice concentration overview of a Sentinel-1A pass that occurred on 1 September 2016 at 06:50 UTC. a) Fractional ice concentration (blue shading) from the daily-average SSMI for Antarctic. The red box represents the region displayed in b). b) Ice concentration (blue shading) and significant wave height in meters from WAVEWATCH III (coloring in the off-ice region). The black boundaries are the SAR acquisitions (to scale). The magenta circles are the images used as examples in Figures S2 and S3.

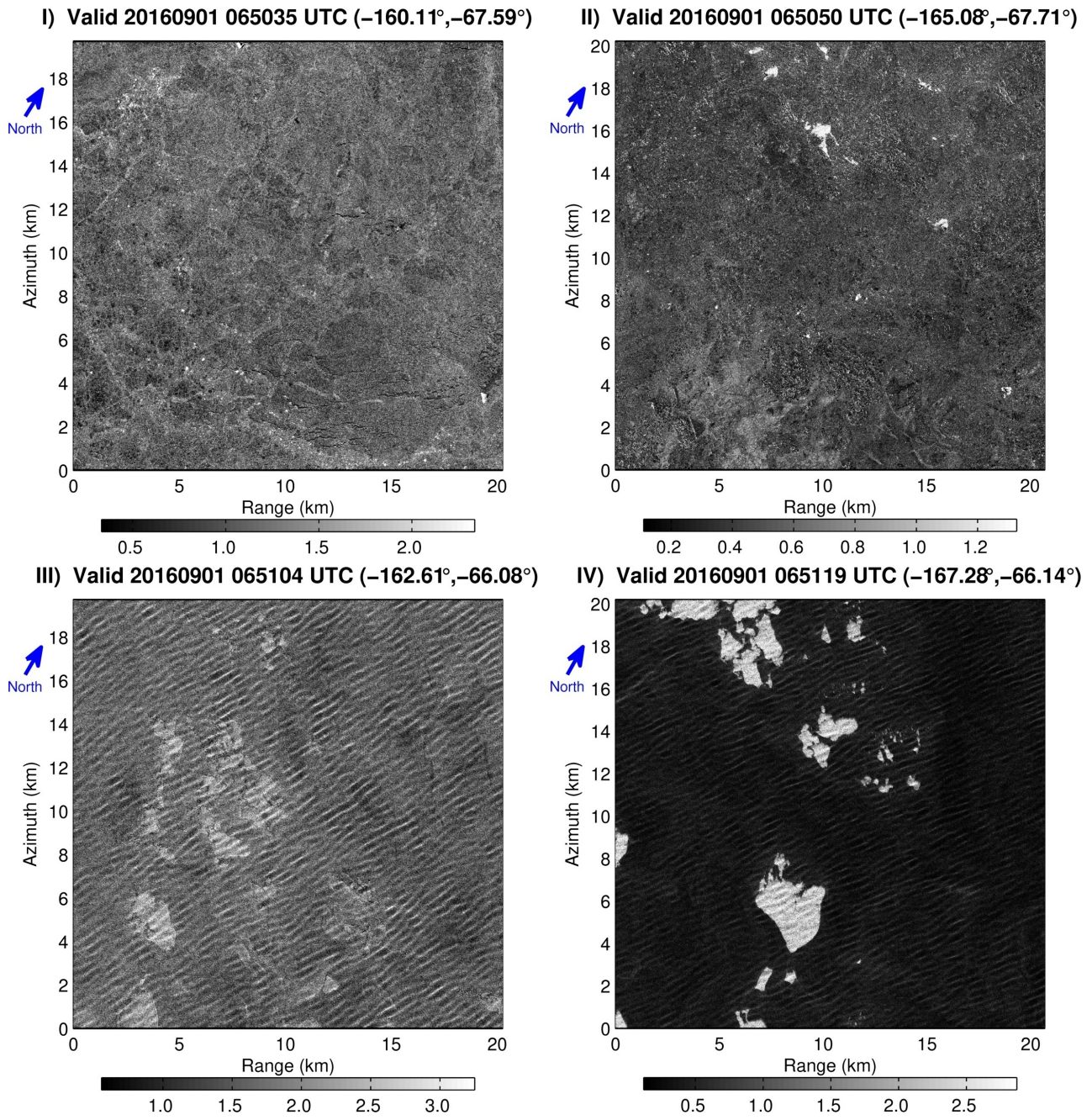


Fig. S2. SAR roughness examples corresponding to the identified acquisitions in Figure S1 (Roman numerals). I and III have incidence angles of 36° (WV2) and II and IV have incidence angles of 23° (WV1).

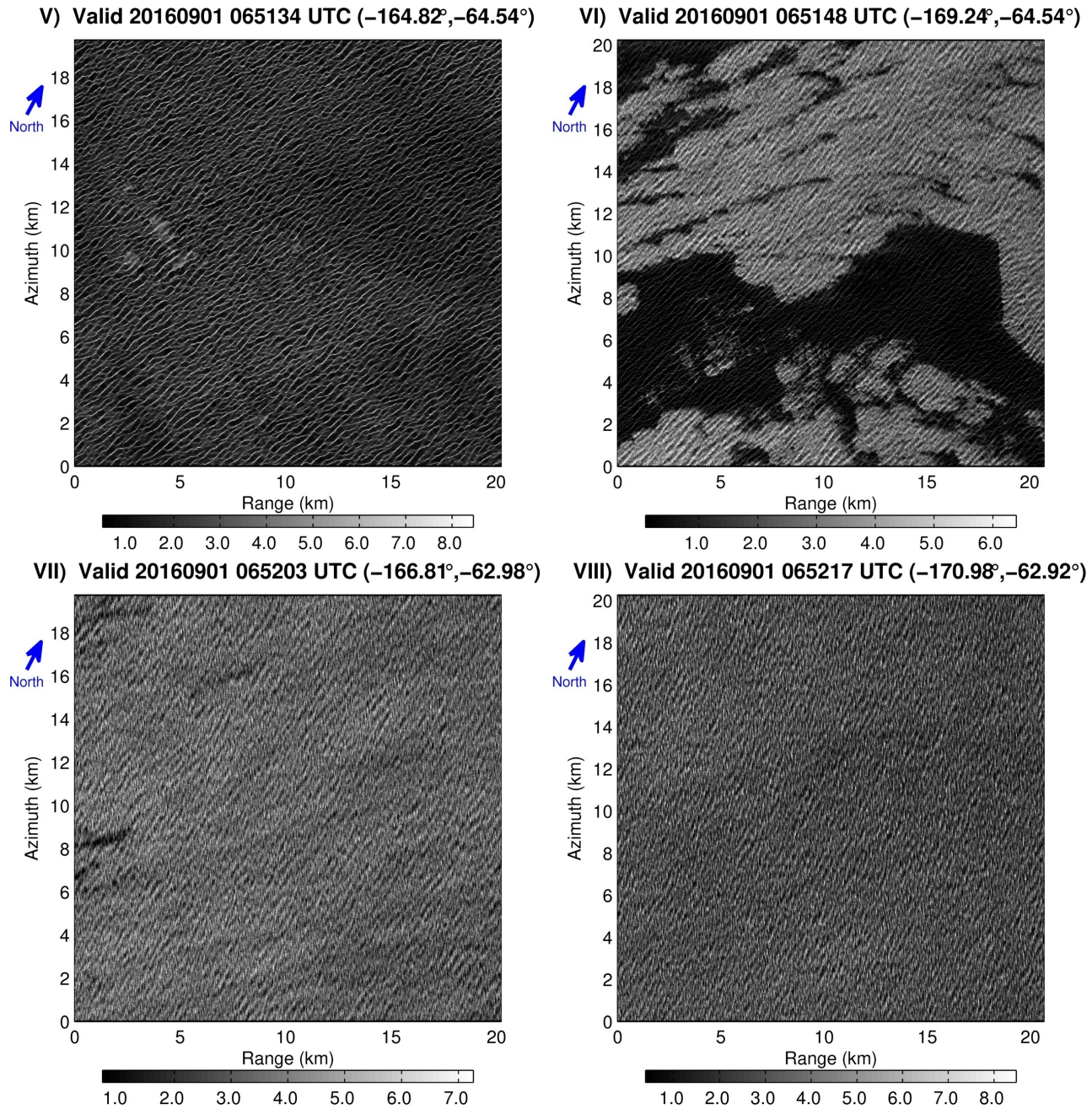


Fig. S3. SAR roughness examples corresponding to the identified acquisitions in Figure S1 (Roman numerals). V and VII have incidence angles of 36° (WV2) and VI and VIII have incidence angles of 23° (WV1).

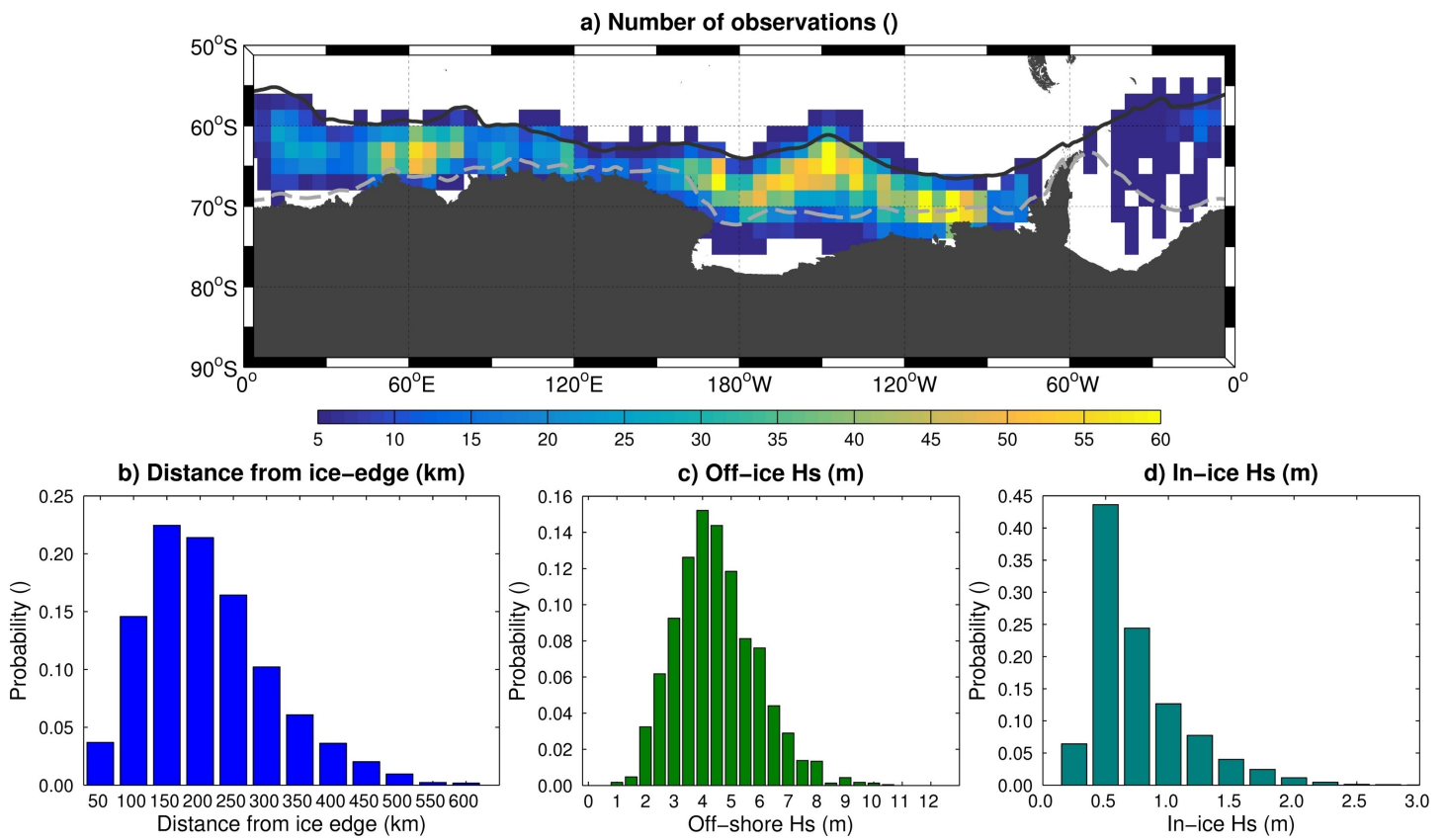


Fig. S4. Statistics of Sentinel-1 A/B SAR observations. a) Number of SAR observations for 4° longitude and 2° latitude bins. The solid black and gray dashed contours represents the August-September-October and February-March-April ice edge from the SSM/I data for 2014-2016 respectively. b) c) d) are probability density functions of the distance from ice edge, off-ice H_s , and in-ice H_s respectively.

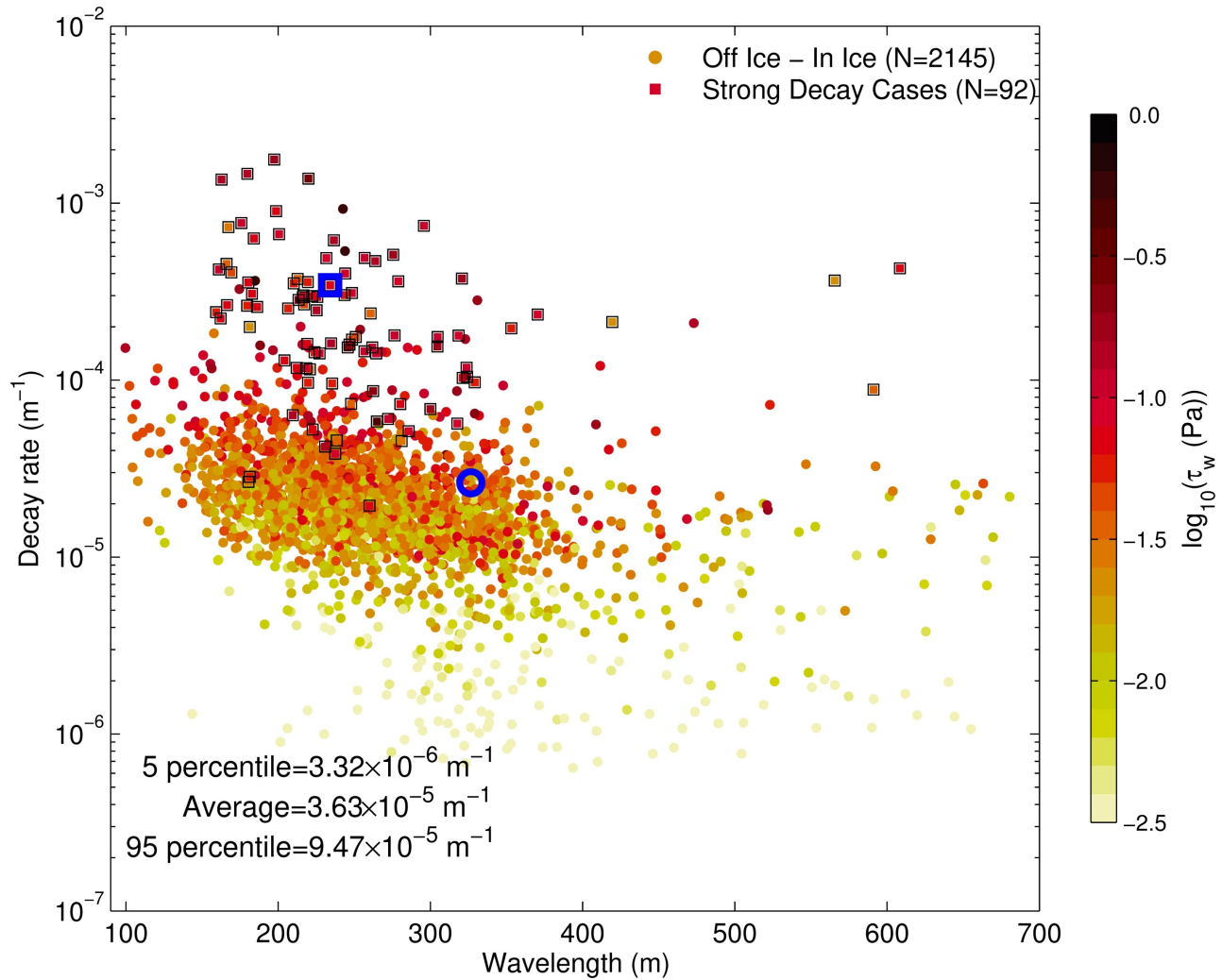


Fig. S5. Wave attenuation and stress: the relationship between the wavelength (abscissa), exponential wave energy decay rate (ordinate), and wave stress (color on logarithmic scale). Squares represent attenuation rates computed within one SAR image (92 cases) and circles represent attenuation rates computed using the gradient between the off-ice and in-ice observations (2145 cases). The blue circle and square correspond Figure 1 a) and d) of the main text respectively. Similar to Figure 2 of the main text except that the off-ice H_s is given by the wave model after back-propagation to ice edge.

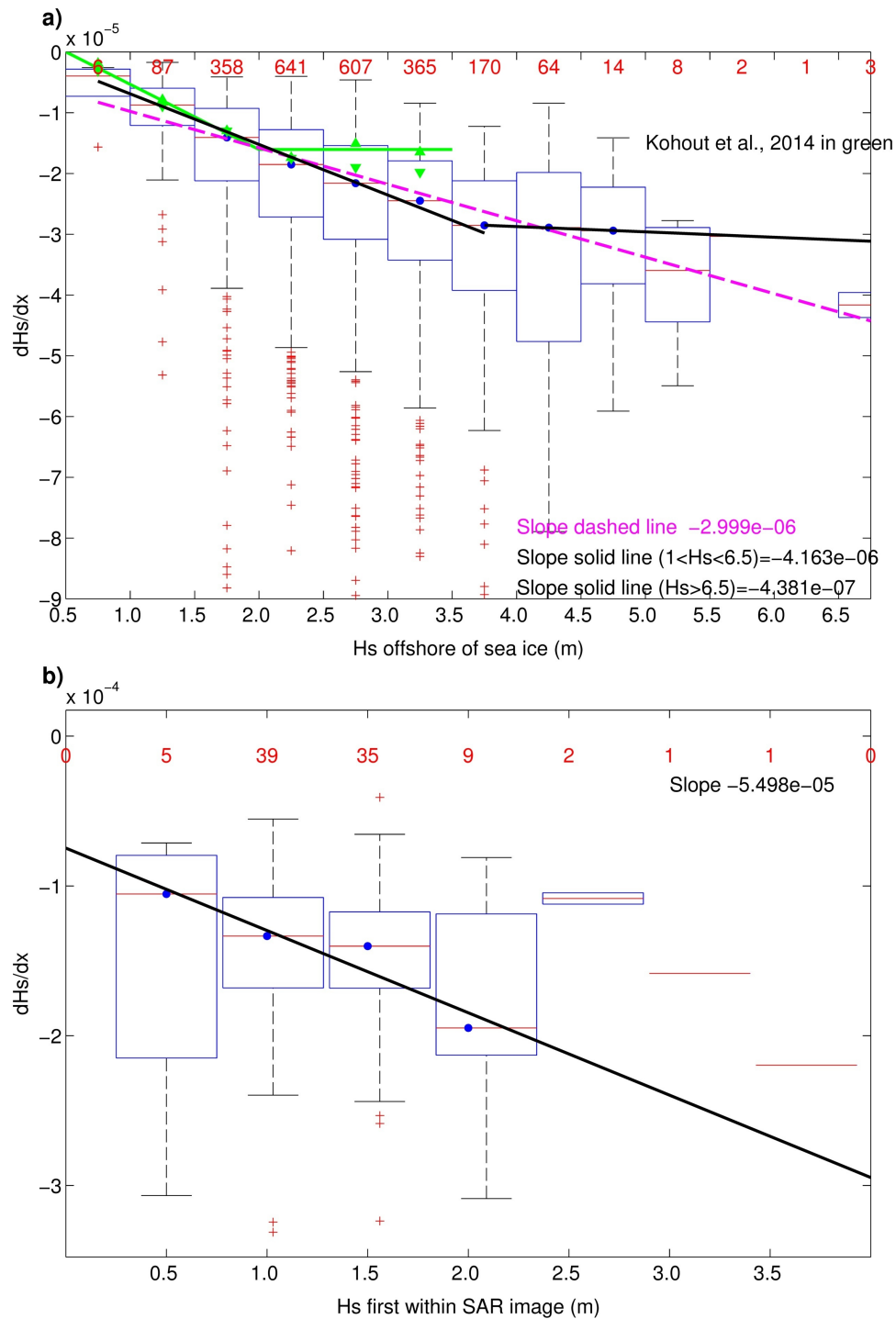


Fig. S6. Wave decay rates a) Computed from off-ice and in-ice pairs plotted as a function of off-ice H_s . Data are binned into 1-m increments. b) Computed from within one SAR image. Data are binned into 0.5-m increments. The blue dots are the medians. The box height shows the inter-quartile range (IQR) (middle 50% of the data). The whiskers show the data range 1.5 times the IQR and typically represents 99% of the data when the data is normally distributed. Values larger than the IQR are identified as outliers and plotted as red plus signs. The solid black lines and magenta dashed line are calculated from a least-squares regression through the median values. The red numbers represent the number of data within each bin. The green triangles and lines represent data from (16).

Table S1. Parameters related to the quality of the SAR inversion corresponding to points in S1 where $Dist$ =distance from ice edge; L_p is the peak wavelength; λ_c is the azimuth cutoff; C_{AR} is the SAR imaging parameter. N/A means not applicable. (+) significant wave height computed using (4). (*) significant wave height computed using the empirical model of (7) values in parenthesis are from WAVEWATCH III.

ID	$Dist$ (km)	L_p (m)	λ_c (m)	C_{AR}	SAR H_s (m)
I	576	N/A	66	0.22	N/A
II	531	N/A	64	0.25	N/A
III	360	402	146	0.28	0.60+
IV	307	370	151	0.43	0.66+
V	183	331	86	0.74	1.65+
VI	78	305	211	1.25	2.83+
VII	N/A	364	374	0.62	7.28*(6.43)
VIII	N/A	339	370	0.56	7.62*(7.11)

References

1. Liu AK, Vachon PW, Peng CY, Bhogal A (1992) Wave attenuation in the marginal ice zone during limex. *Atmosphere-Ocean* 30(2):192–206.
2. Lyzenga DR, Shuchman RA, Lyden JD, Rufenach CL (1985) SAR imaging of waves in water and ice: Evidence for velocity bunching. *Journal of Geophysical Research* 90(C1):1031–1036.
3. Schulz-Stellenfleth J, Lehner S (2002) Spaceborne synthetic aperture radar observations of ocean waves traveling into sea ice. *Journal of Geophysical Research* 107(C8).
4. Arduin F, et al. (2017) Measuring ocean waves in sea ice using sar imagery: A quasi-deterministic approach evaluated with sentinel-1 and in-situ data. *Remote Sensing of Environment*. 189:211–222.
5. Alpers W, Rufenach C (1979) The effect of orbital motions on synthetic aperture radar imagery of ocean waves. *IEEE Transactions on Antennas and Propagation* 27(5):685–690.
6. Engen G, Johnsen H (1995) SAR-ocean wave inversion using image cross spectra. *IEEE Transactions on Geoscience and Remote Sensing* 33(4):1047–1056.
7. Stopa JE, Mouche A (2017) Significant wave heights from sentinel-1 sar: validation and applications. *Journal of Geophysical Research* 122:1827–1848.
8. Stopa JE, et al. (2018) Wave attenuation through an arctic marginal ice zone on 12 october, 2015: 1. measurement of wave spectra and ice features from sentinel-1a. *Journal of Geophysical Research: Oceans*.
9. Koch W (2004) Directional analysis of SAR images aiming at wind direction. *IEEE Transactions on Geoscience and Remote Sensing* 42(4):702–710.
10. Ezraty R, Girard-Arduin F, Piolle JF, Kaleschke L, Heygster G (2007) Arctic and antarctic sea ice concentration and arctic sea ice drift estimated from special sensors microwave data, (Ifremer/CERSAT, ftp.ifremer.fr/ifremer/cersat/products/gridded/psi-drift/documentation/ssmi.pdf), User manual version 2.1.
11. Niedermeier A, Schulz-Stellenfleth J, Lehner S, Nieto-Borge JC (2004) Sar ocean wave measurements based on an empirical imaging model in *Proceedings of the IGARSS conference, Anchorage, Alaska*. pp. 4730–4733.
12. Schulz-Stellenfleth J, König T, Lehner S (2007) An empirical approach for the retrieval of integral ocean wave parameters from synthetic aperture radar data. *Journal of Geophysical Research* 112(C3):C03019.
13. Li XM, Lehner S, Bruns T (2011) Ocean wave integral parameter measurements using envisat ASAR wave mode data. *IEEE Transactions on Geoscience and Remote Sensing* 49(1):155–174.
14. Rasclé N, Arduin F (2013) A global wave parameter database for geophysical applications. part 2: Model validation with improved source term parameterization. *Ocean Modelling* 70:174–188.
15. Wadhams P, Squire VA, Goodman DJ, Cowan AM, Moore SC (1988) The attenuation rates of ocean waves in the marginal ice zone. *Journal of Geophysical Research* 93(C6):6799–6818.
16. Kohout AL, Williams MJM, Dean SM, Meylan MH (2014) Storm-induced sea-ice breakup and the implications for ice extent. *Nature* 509(7502):604–607.
17. Squire V (2007) Of ocean waves and sea-ice revisited. *Cold Regions Science and Technology* 49(2):110–133.